ADVANCED HEALTHCARE MATERIALS
www.advhealthmat.de

Laser-Assisted Micropatterned 3D Printed Scaffolds with Customizable Surface Topography and Porosity for Modulation of Cell Function

Lucia Aboal-Castro, Yago Radziunas-Salinas, Maria Pita-Vilar, Bastian Carnero, Antonios G. Mikos, Carmen Alvarez-Lorenzo, Maria Teresa Flores-Arias, and Luis Diaz-Gomez**

The dynamic interaction between cells and their substrate is a cornerstone of biomaterial-based tissue regeneration focused on unraveling the complex factors that govern this crucial relationship. A key challenge is translating physical cues from 2D to 3D due to limitations in current biofabrication techniques. In response, this study introduces an innovative approach that combines additive and subtractive manufacturing for precise surface patterning of 3D printed scaffolds. Using poly(ε-caprolactone) as the scaffold material, polymeric fibers are 3D printed and subsequently laser-engraved with femtosecond laser to precisely create controlled microtopographies, including microgrooves (10 and 80 µm in width) and micropits (25 µm in diameter). Testing shows that the process does not compromise the mechanical properties of the fibers, which is critical for structural applications in tissue engineering. Human mesenchymal stem cells are used to investigate the effects of these topographical features on cell behavior. The 10 µm wide microgrooves notably enhance cell attachment, with cells aligning in elongated forms along the grooves, while micropits and unpatterned surfaces promote polygonal cell shapes. This combined approach demonstrates that precisely engineered microtopographies on 3D printed scaffolds can better mimic the natural extracellular matrix, improving cellular responses and offering a promising strategy for advancing tissue regeneration.

1. Introduction

The microenvironment, particularly the extracellular matrix (ECM), is pivotal in regulating cellular behavior by influencing factors such as stiffness, topography, and geometry, which in turn activate intricate biochemical pathways.[1,2] Cellular responses encompass an array of interconnected complex functions, including cell adhesion, shape, proliferation, and migration.[3] Understanding cell–substrate interactions is fundamental to tissue engineering, where scaffolds are designed to mimic the in vivo microenvironment, supporting processes like cell adhesion, proliferation, and differentiation.[1,4] While significant progress has been made in studying cell responses to topographical cues on 2D surfaces, translating these findings to 3D scaffolds remains challenging due to the complex methodologies involved in fabricating precise surface patterns.[5]

Beyond topography, the 3D structure of scaffolds also plays a crucial role in cell behavior, including migration, proliferation,

L. Aboal-Castro, M. Pita-Vilar, C. Alvarez-Lorenzo, L. Diaz-Gomez
Department of Pharmacology
Pharmacy, and Pharmaceutical Technology
I+D Farma (GI-1645)
Facultad de Farmacia
and Health Research Institute of Santiago de Compostela (IDIS)
Universidade de Santiago de Compostela
Santiago de Compostela 15782, Spain
E-mail: luis.diaz.gomez@usc.es

The ORCID identification number(s) for the author(s) of this article can be found under https://doi.org/10.1002/adhm.202403992

DOI: 10.1002/adhm.202403992

L. Aboal-Castro, Y. Radziunas-Salinas, M. Pita-Vilar, B. Carnero, C. Alvarez-Lorenzo, M. T. Flores-Arias, L. Diaz-Gomez
Instituto de Materiales (iMATUS)
Universidade de Santiago de Compostela
Santiago de Compostela 15782, Spain
E-mail: maite.flores@usc.es

Y. Radziunas-Salinas, B. Carnero, M. T. Flores-Arias
Photonics4Life Research Group
Applied Physics Department
Facultade de Física and Facultade de Óptica e Optometría
Universidade de Santiago de Compostela
Campus Vida, Santiago de Compostela 15782, Spain

A. G. Mikos
Department of Bioengineering
Rice University
Houston, TX 77030, USA

and gene expression. Accurately mimicking microenvironmental cues in scaffolds is critical for the precise regulation of cellular fate.[6] Natural tissue-like structures, as well as intercellular signaling, are enhanced when cells are supported on 3D scaffolds, which can be finely tuned to reproduce the unique features of the ECM through additive manufacturing technologies.[7,8] Although biopolymer-based hydrogels are commonly used for studying cell-ECM interactions in a 3D setting, they exhibit rapid biodegradation and reorganization, complicating long-term evaluations of effects of the topography on cells.[9] As an alternative, 3D scaffolds prepared from synthetic polymers, ceramics, or metals may offer complementary possibilities for enhanced stability and functionality.

Existing fabrication methods, such as salt leaching, etching, and thermally induced phase separation, often lack the spatial control needed to produce microscale features in 3D constructs and face challenges with reproducibility and scalability.[10] Techniques like soft lithography and chemical etching can be labor-intensive and involve toxic chemicals, limiting their applicability in creating intricate 3D structures for biomedical applications.[11] Therefore, there is a need for advanced biofabrication methods that enable precise, reproducible microscale patterning of 3D scaffolds, essential for directing cellular behavior in tissue engineering applications.[10,12]

Laser-assisted engraving has been used to create patterned topographies with high resolution and precision on 3D printed scaffolds.[13] This approach is particularly advantageous for fiber engraving due to its contactless, non-contaminant, and single-step nature, eliminating the need for chemicals or sacrificial materials. However, challenges arise especially with heat-sensitive materials like polymers, where substrate properties and thermal behavior significantly influence ablation outcomes. Careful selection of laser wavelength, pulse duration, and processing parameters is required to optimize light-matter interaction and prevent excessive energy buildup that could damage the substrate. [14,15] Femtosecond lasers address these issues by depositing energy within ultrashort time frames, allowing direct vaporization via non-linear interactions and significantly reducing debris redeposition.[16,17] However, high repetition rates must be carefully managed to prevent thermal effects that could compromise the integrity of the material.[18]

Ultrashort pulse lasers thus offer enhanced precision, efficiency, and flexibility enabling high-resolution surface patterning while maintaining surface integrity.[19] These attributes make ultrashort-scale techniques particularly promising for tissue engineering applications, where replicating the micro to nano-scale features of the natural ECM is essential.[15,17,20–22] However, surface accessibility is a limitation in traditional laser engraving, as it typically targets only upper scaffold layers, leaving deeper regions unpatterned. This limitation impedes the creation of intricate patterns throughout the scaffold entire volume. Moreover, surface degradation and debris accumulation around engraved areas can reduce scaffold quality and functionality.

This study presents a novel fabrication approach that integrates additive and subtractive manufacturing by combining 3D printing with femtosecond laser engraving. This integrated method addresses limitations in current techniques, allowing for the reproducible creation of high-resolution surface patterns without compromising the scaffold's structural integrity or mechanical properties. The 3D printing stage fabricates porous scaffolds, while layer-specific femtosecond laser engraving introduces controlled surface topographies, including 10 or 80 µm microgrooves and 25 µm micropits. Pattern consistency was assessed to ensure reproducibility, and mechanical and thermal properties of the engraved scaffolds were evaluated. Finally, the influence of these patterns on human mesenchymal stem cell (hMSC) attachment, proliferation, and morphology was explored, highlighting the potential for these scaffolds to guide cell behavior and promote tissue regeneration.

2. Results and Discussion

2.1. Scaffold Fabrication and Characterization

In this study, PCL scaffolds with three different topographies were developed using an innovative additive/subtractive manufacturing methodology. After the printing of each layer, the surface of the deposited fibers was engraved using a femtosecond laser, as depicted in **Figure 1**. Three different surface patterns were applied to 3D-printed PCL fibers: parallel grooves with widths of 10 µm and 80 µm along the fiber direction, and micropits with a diameter of 25 µm. Non-engraved scaffolds (PCL-C) served as controls. This approach is advantageous as it eliminates the need for incorporating porogens or sacrificial materials, and avoids the drawbacks of uncontrolled post-printing processes like solvent etching, which can lead to variability in the resulting topographical features.[10,23,24] Also, micropatterning was applied only to the top surface of the scaffolds, with the remaining surface left unpatterned to serve as internal controls. This design allows for a direct comparison between patterned and non-patterned surfaces within the same structure, offering insights into the effects of topographical cues on cell behavior under identical conditions. Additionally, having an unpatterned control surface with direct access for microscopy enables the assessment of cells in both conditions simultaneously, improving the significance of the experimental data.

PCL was selected as the printing material for its mechanical strength, biocompatibility, and widespread use in tissue engineering applications.[25] Using layer-by-layer printing, the deposition of single material compositions within a consolidated structure was precisely achieved, preserving both the geometry and porosity of the scaffolds while ensuring efficient production times.

SEM (**Figure** 2A–H) and microCT (Figure 2I–L, Videos S1–S3 and Figure S1, Supporting Information) analyses revealed that the overall shape of the scaffolds remained intact, with the engraved patterns affecting only the upper surface of the fibers where they were applied. The engraving was consistent along the length of the fibers, aligning precisely with their central axis and maintaining high fidelity to the designed CAD model. The precise XY control of the laser beam enabled consistent spatial distribution of the micropatterns, effectively addressing the misalignment issues commonly encountered in already established techniques, such as template engraving.[26] The grooved patterns (PCL-G10 and PCL-G80) exhibited distinct parallel microgrooves with well-defined edges. The PCL-MP scaffolds displayed cylindrical pores with clearly defined edges, which were homogeneously distributed along the surface of the fibers.

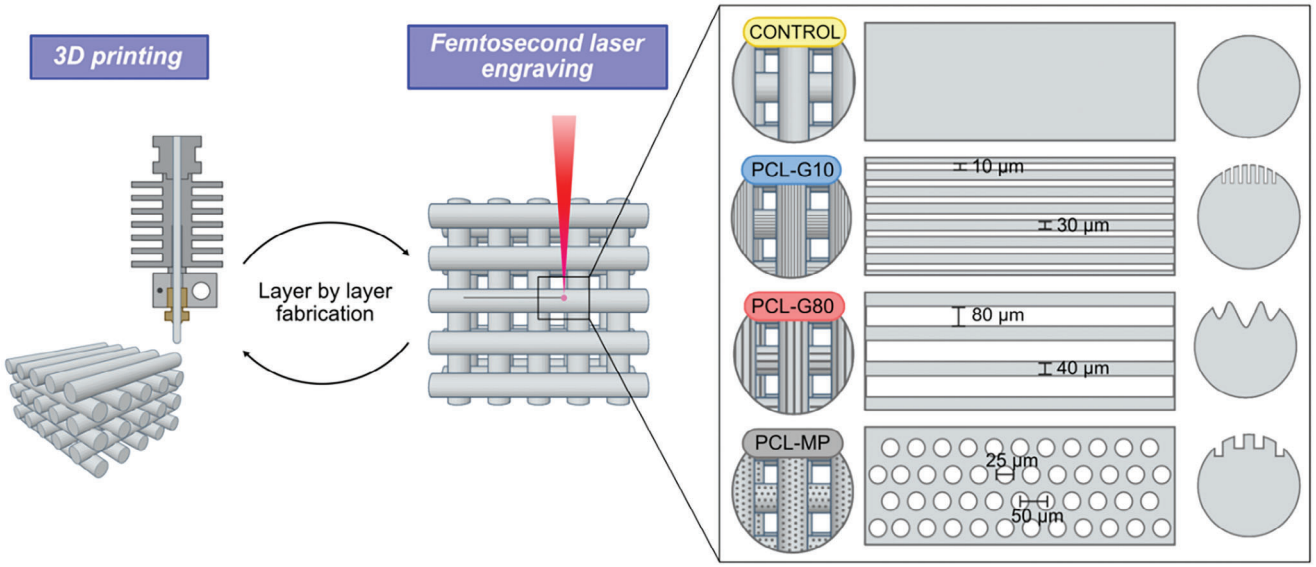

Figure 1. Schematic representation of the biofabrication process showing the 3D printing of PCL fibers, followed by sequential femtosecond laser ablation steps after solidification of each layer. These steps were repeated until the scaffold manufacturing was completed, resulting on precise micropatterns on the fiber surfaces, including 10 µm (PCL-G10) and 80 µm (PCL-G80) grooves, and micropits (PCL-MP). Non-engraved scaffolds were used as controls (PCL-C).

The depth and width of the engraved patterns were measured using microCT (Figure 2M). Assessments at layers 2, 4, and 6 demonstrated the reproducibility of engraving across different printed layers. All engraved fibers exhibited widths closely matching the CAD patterns. Specifically, the PCL-G10 and PCL-G80 scaffolds had average groove widths of 10.0 ± 0.8 and 80.2 ± 4.7 µm, respectively. The PCL-MP scaffolds showed an average micropit diameter of 26.7 ± 2.1 µm. No significant differences were found in the widths of the engraved patterns throughout the height of the layers, confirming that the reported method provides solid reproducibility regardless of the engraved layer height. The overall engraved widths on each fiber, incorporating both pattern arrays and spacing between them, were 265 ± 4 µm for PCL-G10, 339 ± 19 µm for PCL-G80, and 232 ± 4 µm for PCL-MP.

While the width of the engraved patterns can be precisely adjusted in the CAD model, the depth is determined by the ablation setup. As reported in the literature, the depth of each engraved pattern increases with the number of pulses per unit area, which is controlled by the scan speed.[14,27,28] In this study, a speed of 1 mm s^{-1} was selected to ensure good overlap and create continuous, regular grooves. Therefore, the engraving time can be directly calculated from the length of the engraved area, allowing for precise control over processing duration based on the desired pattern dimensions. Each groove is 8 mm long, with PCL-G10 scaffolds having 7 grooves per fiber, resulting in an engraving time of approximately 56 s per fiber, or ca. 10 min per layer. In contrast, PCL-G80 scaffolds have 3 grooves per fiber, leading to a total engraving time of approximately 24 s per fiber, or ca. 5 min per layer. The PCL-MP scaffolds feature four arrays, each containing 160 micropits per fiber, with each micropit requiring approximately 200 laser pulses at a 1 kHz repetition rate. This setup results in a total engraving time of approximately 30 min per layer. While a higher repetition rate could significantly reduce the engraving time, the femtosecond laser available in our facility operates at a fixed 1 kHz.

The power reaching the sample for each configuration was optimized to achieve the desired widths of the engraved patterns. For PCL-G10 scaffolds, an applied power intensity of 9.2–9.5 mW with repetition pulses (ν = 1 kHz) resulted in shallow grooves with an average depth of 27.7 ± 2.6 µm. Conversely, PCL-G80 scaffolds required 92–94 mW of power, yielding an average depth of 48.0 ± 14 µm. PCL-MP scaffolds were engraved with a power intensity of 42 mW, resulting in an average depth of 266.3 ± 9.9 µm.

The overall widths of the micropatterns, including grooves and micropits as well as the spacing between them, were determined to be 265 ± 4, 339 ± 19, and 232 ± 4 µm for PCL-G10, PCL-G80, and PCL-MP, respectively. Also, the shape of the engraved pattern varied with each condition: the 10 µm grooves had a rectangular shape, the micropits were cylindrical, and the 80 µm grooves exhibited a triangular geometry due to the Gaussian distribution of the laser beam (Figure 2J–K). The higher power used to obtain 80 µm grooves resulted in a shape closer to the Gaussian beam footprint. For PCL-G80, higher power levels compared to PCL-G10 allowed a larger portion of the beam to exceed the ablation threshold, producing a Gaussian-like profile. In contrast, the rectangular profile in the 10 µm grooves resulted from a smaller area of the beam surpassing the ablation threshold. In PCL-MP engraving, the diameter and depth of the micropits were directly related to the pulse energy and the number of pulses applied per pit. The circumferential shape of the pits corresponded directly to the Gaussian beam footprint on the sample.

Both SEM and microCT analyses (Figure 2A–L) confirmed that no other areas within the engraved region were affected. The absence of debris was attributed to the femtosecond laser ablation process: the short pulse duration results in extremely high intensity, allowing for precise removal of atoms from the surface

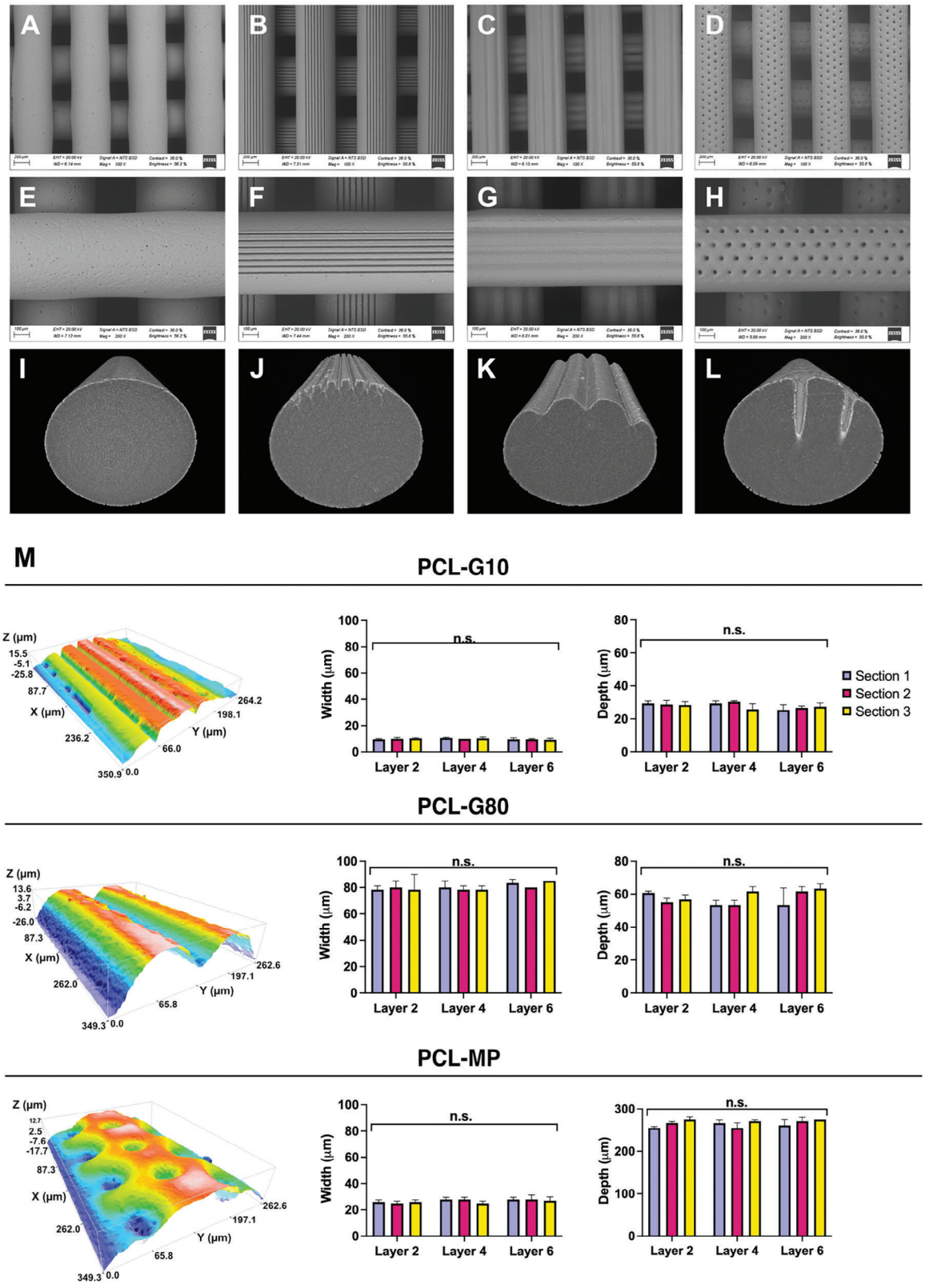

Figure 2. Structural characterization of engraved scaffolds including SEM micrographs of the surface of A–H) PCL-C, PCL-10, PCL-80, and PCL-MP scaffolds and I–L) microCT reconstructions of single fibers. M) 3D profiles of the engraved fibers, obtained using optical profilometry (left) and evaluation of the depth and width measurements on layers 2, 4 and 6 (right).

of the printed fibers. Free electrons in the sample absorb laser energy, surpassing the Fermi energy, which intensifies material removal due to the electric field created between the parent ions and escaped electrons. Because of the femtosecond pulse duration, heat diffusion is negligible, with interaction times between surface electrons and the phonon structure occurring in the picosecond range, thus avoiding hydrodynamic motion.[29,30] This results in smooth ablation profiles with well-defined borders, indicating the absence of expelled polymer residues, as evidenced in the PCL-G80 and PCL-G10 scaffolds.

Regarding PCL-MP engraving, two critical factors influence the shape and smoothness of the pits. First, energy affects the pit diameter, influencing the footprint of the Gaussian beam profile. Second, the number of pulses per pit determines the pit depth. According to the literature, using a sufficient number of pulses (greater than $N = 100$) results in a smooth engraving, preventing remelting of expelled material at the pit edges, as the repetition rate allows complete evaporation of the material when pulses are sufficiently high.[14,31] With fewer pulses, more intense ejections can lead to material accumulation at the edges, increasing surface roughness and compromising the cleanliness of the resulting patterned topographies.

Laser patterning has been previously applied in biomaterial research, yet the integration of this subtractive technique with 3D printing presents a notable advancement in precision and micropatterning capabilities. While the engraving of 3D printed scaffolds prepared from biodegradable polymers, including PCL, poly(lactic acid), and poly(L-lactic acid), has led to modified surface topographies, previous methodologies often resulted in significantly lower engraving resolution and were limited to the upper layers of the scaffold.[17,20,13] Conversely, the methodology described in this study resulted in the precise surface patterning of the PCL scaffolds with negligible heat diffusion and debris to the surrounding areas, avoiding undesirable fiber irregularities. Techniques that enable microtopographical tuning generally require multiple processing steps and often lack the precision necessary to control patterns or topographical cues at a highly detailed level. Specifically, traditional methods for micropatterning polymers, such as chemical etching, sacrificial layer techniques, stereolithography, and selective laser melting, each have unique limitations, as previously discussed in detail.[11] For instance, SLA is typically restricted to photocrosslinkable polymers and the biocompatibility of photopolymerizable inks is limited.[32] In contrast, the integration of 3D printing with femtosecond laser engraving used in this study allows for an efficient, single-step process that achieves high-resolution microgrooves and micropits on FDA-approved biopolymers. Significantly, this process does not compromise the mechanical stability of the scaffold compared to other techniques like salt leaching, which is crucial for biomedical applications.[33] The ability to precisely control topographical features without sacrificing biocompatibility or structural integrity is particularly beneficial for tissue engineering applications.

As stated in the literature, employing nanosecond or picosecond pulse lasers often leads to more irregular outcomes, primarily due to electron-phonon interactions that generate heat-affected zones and increased melting and vaporization of materials.[34] Under this paradigm, when a pulse irradiates a solid sample, most of the energy accumulates on its surface, resulting in an increase of the surface temperature as well as the appearance of an energetic diffusion into the material. Electron-phonon interactions cause a significant increase in the sample's surface temperature, accelerating the atoms in that region, leading to the evaporation and boiling in the sample when overcoming bonding forces. This generates a thin layer in the material, which marks the beginning of ablation and plasma creation, called plume. The appearance of the plume results in to changes in the interaction mechanisms, leading to intense energy transport phenomena to be induced in the vicinity of the surface, so that the solid layer of thermal penetration meets excess liquid and gaseous material, yielding to the appearance of the recast layer and debris, as well as the thermic stress of the sample. In contrast, femtosecond laser engraving enables high-precision engraving without compromising the integrity of the scaffolds.[34]

2.2. Differential Scanning Calorimetry (DSC)

DSC analysis was carried out to evaluate the effect of the engraving process on the crystal structure of the PCL scaffolds, as summarized in **Table 1**. PCL scaffolds showed a melting peak at ca. 60 °C. Similar thermal behaviors were observed for engraved scaffolds (PCL-G10, PCL-G80 and PCL-MP). The degree of crystallinity (*X*c) for PCL-G10 and PCL-G80 was 57.5% and 58.1%, respectively while PCL-MP and PCL-C crystallinity was 48.4% and 52.1%, respectively. Melting temperature (*T*m) was similar for all scaffolds (Table 1), which confirmed that the applied engraving process had no influence on the bulk structure of the final material. Previous studies reported that the crystal structure of polyesters could be altered depending on the ablation methodology.[35,36] Specifically, changes in the degree of crystallinity could also be related with material expulsion from the scaffold surface during ablation, which can alter intermolecular forces and monomer cross-linking of the crystalline structure throughout irradiation and eventually modify the PCL polymorph.[37]

2.3. Gel Permeation Chromatography (GPC)

The number average molecular weight (*M*n) and weight average molecular weight (*M*w) of PCL scaffolds were determined using GPC (Table 1). The *M*w of the polymer in PCL-C, PCL-G10, and PCL-G80 scaffolds remained consistent at approximately 80 kDa, confirming that the engraving process did not significantly affect the *M*w despite the laser power used ($p > 0.05$). On the contrary, PCL-MP scaffolds showed a decreased *M*w of ca. 72 kDa, which could be attributed to the higher energy, repetition pulses, and depth of the engraving. Similarly, the *M*n of PCL remained stable at around 40 kDa across all groups except for PCL-MP, that resulted in an average *M*n of ca. 35 kDa.

2.4. Mechanical Properties

The tensile tests were carried out following an adapted methodology as described in the ASTM D638−22 standard.[38] The tensile modulus of the PCL-C was 353.0 ± 27.5 MPa. Similarly, engraved fibers showed a tensile modulus of 360.0 ± 20.8 MPa for

Table 1. Summary of DSC and GPC results for engraved (PCL-G10, PCL-G80, PCL-MP) and non-engraved (PCL-C) scaffolds.

Scaffold	T_m [°C]	ΔH_m (1st cycle) [J g^{-1}]	ΔH_m (2nd cycle) [J g^{-1}]	Crystallinity [%]	M_w [kDa]	M_n [kDa]
PCL-C	66.7	72.6	67.3	48.2	78.1	41.9
PCL-G10	65.5	79.5	64.1	57.5	80.8	40.8
PCL-G80	65.3	80.4	67.9	58.1	81.2	43.3
PCL-MP	64.1	69.4	57.6	48.4	72.7	35.5

PCL-G10, 360.7 ± 31.0 MPa for PCL-G80, and 366.7 ± 23.0 MPa for PCL-MP fibers (**Figure** 3A). The results showed that the engraving process did not significantly affect the tensile strength of the fibers ($p > 0.05$). The selection of appropriate engraving parameters enables precise control over the process, allowing for surface modifications without depositing debris, while simultaneously preserving the mechanical properties of the scaffold.

2.5. Stability of Micropatterned Scaffolds

The stability of the engraved patterns was assessed by immersing the samples in PBS for 14 d at 37 °C. The width and depth of the engraved micropatterns showed no significant differences ($p > 0.05$) between layers after immersion in PBS (Figure 3B). Similarly, there were no significant differences in pattern dimensions compared to day 0 ($p > 0.05$), indicating that the dimensions of the patterns remained stable during in vitro incubation. Water adsorption, swelling, and debris generation can potentially alter the superficial features of the engraved scaffolds, leading to blurring, loss of resolution, and gradual variations in pattern dimensions.[39] However, the slow degradation rate of PCL compared to other polyesters helps preventing changes in the porous structure, thereby maintaining the topography of the printed scaffolds over extended periods.[40,41] This stability is crucial for studying cell-material interactions, as it ensures that the physical properties of the scaffolds remain consistent throughout the study.[42,43]

2.6. hMSC Attachment and Proliferation

Cell attachment was assessed through software-assisted nuclei counting on confocal micrographs taken after 24 h of culture (**Figure** 4A–D). The results were normalized to the area of the engraved patterns or corresponding non-engraved regions to evaluate the impact of the topography on hMSC attachment (Figure 4E). PCL-G10 scaffolds demonstrated significantly higher cell attachment compared to PCL-C scaffolds, as well as PCL scaffolds with larger grooves (PCL-G80) and micropits (PCL-MP). The enhanced hMSC attachment observed on PCL-G10 scaffolds could be attributed to the specific effects of surface roughness on cellular adhesion.

Concave roughness features, such as the 10 µm grooves on PCL-G10 scaffolds, play a pivotal role in enhancing cell attachment. The grooves on PCL-G10 closely match the scale of focal adhesions and integrins, facilitating robust cellular interactions with the substrate by providing an optimal surface for focal adhesion complex formation, which is essential for establishing strong cell-material connections.[44] In addition, grooves in the 10 µm width range could increase capillary forces compared to wider grooves, further promoting cell adhesion.[45] In contrast, larger V-shaped grooves like PCL-G80 scaffolds can impede cellular interactions by creating uneven surfaces where focal adhesions may concentrate at the groove edges, potentially disrupting uniform cell attachment and actin stress fiber alignment. Grooves wider than 10 µm might make it difficult for cells to bridge the spaces, leading to fewer and less stable focal adhesions, and reduced ECM formation. Non-engraved fibers, lacking these specific surface features, also show lower levels of cell attachment due to the absence of enhanced focal adhesion sites and ECM accumulation.[46]

The aspect ratio of the nuclei was significantly lower in PCL-G80 scaffolds, likely due to the increased surface area within the groove walls compared to the curved surface of the ridges of the fibers of the PCL-G10, PCL-MP scaffolds and the PCL-C controls (Figure 4F). The larger surface area in PCL-G80 scaffolds may contribute to a more spread-out and flattened nuclear morphology without significantly impacting Feret´s diameter (Figure 4G). Contrarily, sphericity was significantly higher on cells attached to grooved scaffolds (PCL-G10 and PCL-G80) than those attached on controls and micropits (PCL-C and PCL-MP, respectively) (Figure 4H). Grooved patterns create concave regions on the fiber surfaces, influencing the mechanical environment of the attached cells. When cells adhere to these concave areas, the positioning leads to a mechanical relaxation of the nucleus that could be attributed to the spatial arrangement of cell-substrate adhesions. On flat surfaces, stress fibers tend to generate more significant compressive forces on the nucleus due to the planar distribution of adhesions.[47] in contrast, the concave geometry of grooved fiber surfaces may reduce the compressive load on the nucleus, as it disrupts this planar stress distribution. These findings are consistent with previous studies on 2D substrates with 3D microtopographies, which have demonstrated that the curvature of the substrate can influence cellular morphology and mechanical stress distribution.[48] This could have important implications for cellular functions such as gene expression, proliferation, and differentiation, which are known to be influenced by nuclear shape and mechanics.

Cellular response was further evaluated by monitoring hMSC proliferation after 1 and 3 d of culture on the scaffolds using a CCK-8 assay. Therefore, cell viability was quantified throughout the scaffold, not just at the surface (Figure 4I). The results, represented as a percentage relative to the negative control (PCL-C), showed a significant increase in cell proliferation in grooved scaffolds after 1 d of culture. Specifically, PCL-G10 scaffolds exhibited

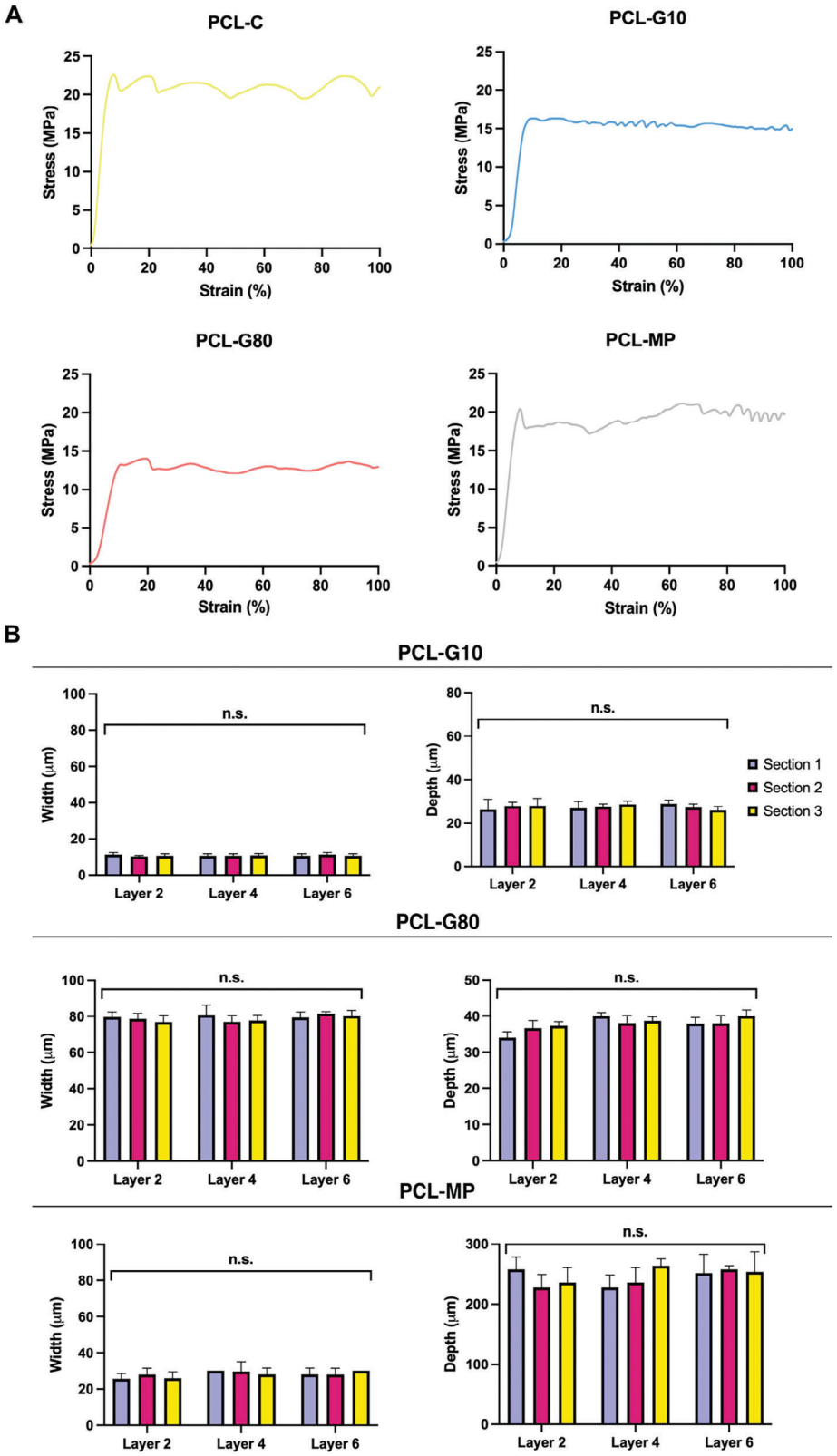

Figure 3. A) Tensile mechanical properties of engraved samples, including load-displacement curves of PCL-C, PCL-G10, PCL-G80 and PCL-MP fibers; and B) dimensions (width and depth) of the engraved patterns on layers 2, 4, and 6 of scaffolds after incubation in PBS for 14 d at 37 °C.

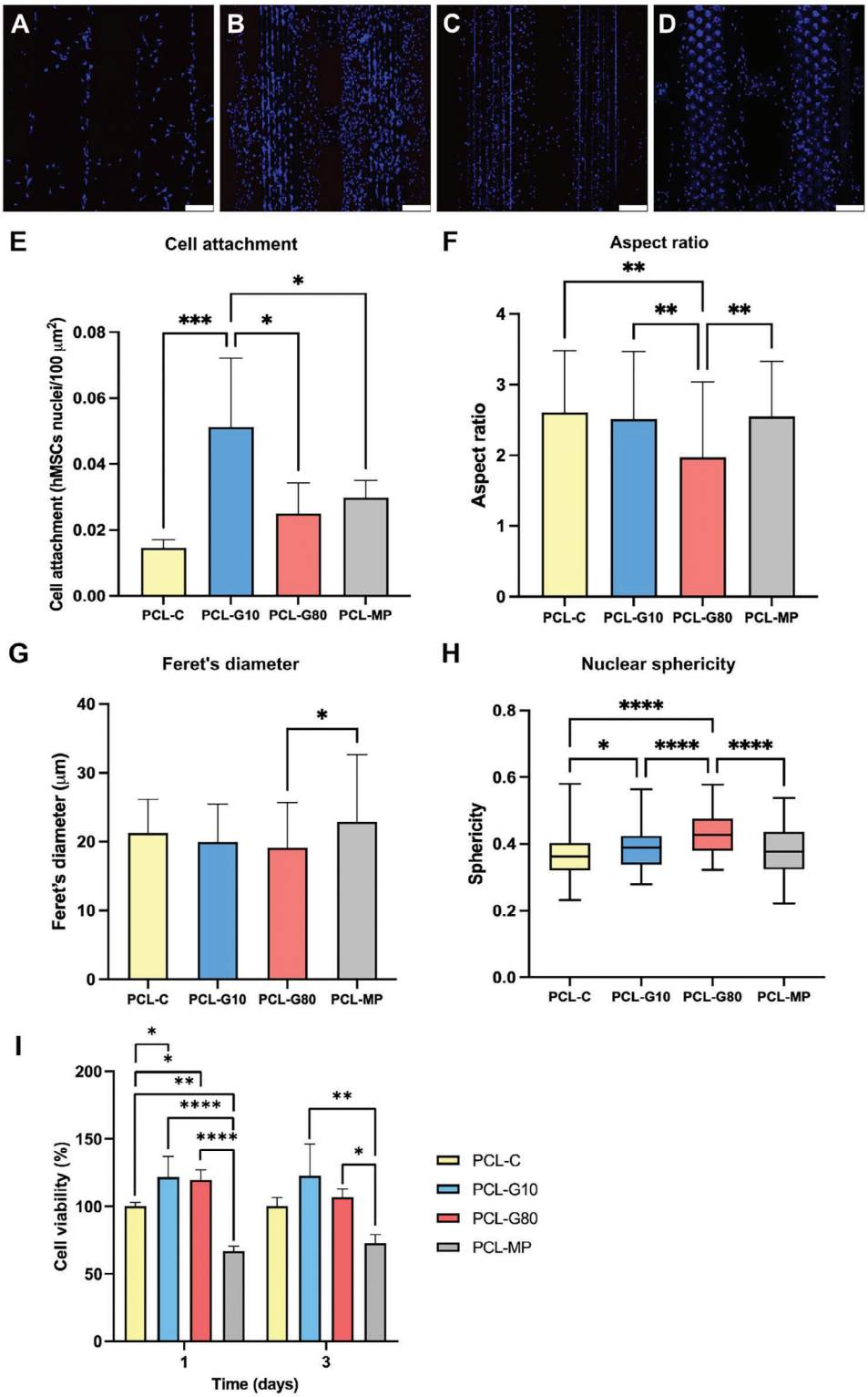

Figure 4. Results from quantification of hMSC attachment. A–D) Micrographs corresponding to 24 h of after seeding on PCL-C, PCL-G10, PCL-G80 and PCL-MP scaffolds, respectively. Scale bar: 200 μm. E) Cell attachment, represented as the number of hMSCs per 100 μm^2. F) Aspect ratio, G) Feret's diameter and H) Sphericity of hMSC nuclei on engraved and non-engraved scaffolds (n = 60 for each condition). I) Cell viability of PCL-C, PCL-G10, PCL-G80 and PCL-MP scaffolds after 1 or 3 d of culture. Results are expressed as percentage of cell viability relative to PCL-C scaffolds (unengraved controls). Data reported as mean ± standard deviation (SD) (* $p < 0.01$, ** $p < 0.01$, *** $p < 0.001$ and **** $p < 0.0001$). Lines in the box–whiskers plot display the following values: lower line, 25th percentile; middle line, median; upper line, 75th percentile; lower whisker, minimum; upper whisker, maximum.

the highest cell viability (121.77% ± 15.36), while PCL-G80 scaffolds (119.53 ± 7.38%) also supported a significant cell viability compared to the unengraved control (PCL-C). By day 3, the differences in cell viability observed initially were reduced, with no significant differences detected between the PCL-G10 and PCL-G80 scaffolds and the unengraved PCL-C control. Conversely, PCL-MP scaffolds (66.67 ± 3.74%) showed decreased cell viability at both 1 and 3 d of culture, likely due to the restricted cell spreading observed in the confocal images. The micropits engraving on PCL-MP scaffolds may limit cell attachment and elongation, resulting in sub-optimal cell-substrate interactions and focal adhesion formation.[49]

2.7. hMSC Organization

Cells can adapt their morphology and orientation in response to external physical stimuli, including substrate topography. To assess this adaptation, hMSCs seeded on both engraved and control scaffolds were analyzed by measuring the orientation of the major axis of their cytoplasm relative to the direction of the printed fiber and cytoplasm aspect ratio after 1, 3, and 7 d of culture (Figures S2–S4, Supporting Information). Differences in cell morphology became apparent as early as 24 h of culture, illustrating the immediate impact of the scaffold topography on cellular behavior. Cells on PCL-G10 scaffolds exhibited a significantly higher aspect ratio, indicating greater elongation, compared to those on the other scaffolds (**Figure** 5A,C). This elongation was consistent across all time points, reflecting an enduring alignment of cell morphology with the 10 µm grooves, as shown in the orientation analysis (Figure 5D). In contrast, cells on PCL-C and PCL-MP scaffolds initially showed no preferred orientation and maintained a rounded morphology similar to cells on well plates. The absence of topographical features in the micropits and non-engraved scaffolds did not provide directional cues for cell orientation at initial culturing times. However, some organization was observed by day 7, likely due to increased cell density, which may have influenced cells to adopt a more organized arrangement despite the lack of explicit directional cues.

Cells on non-engraved PCL-C scaffolds displayed a random orientation throughout the culture period, confirming that the absence of topographical features does not guide cell alignment. PCL-MP scaffolds did not promote cell elongation, displaying a random cell distribution similar to non-engraved scaffolds. This behavior can be explained by two simultaneous phenomena occurring on this specific topography. Firstly, cells adhering within the micropits maintain their viability while adopting a rounded morphology. In this study, the depth of the micropits greater than the size of the cells effectively confines the cells within these pits. In contrast, in less-deep micropits, cells exhibit more freedom of movement, potentially leading to more elongated morphologies.[50] Secondly, cells that adhere and proliferate on the flat inter-micropit surfaces (ridges) of the engraved fibers exhibit a randomly oriented shape. The presence of micropits disrupts the continuous surface, leading to a random orientation of the cells as they adapt their cytoplasm around these surface convexities. This observation could be also related to the lower cell viability described in the proliferation study (Section 2.6). Unlike grooves, micropits do not provide directional topographical cues that guide cell orientation and elongation, resulting in a lack of uniform cell alignment.[51] Additionally, the presence of micropits may cause variations in local stiffness and mechanical signals, similar to micropillars, causing cells to deform and further contributing to the random distribution of cell orientation.[52]

Consistent with previous studies carried out on 2D substrates, PCL-G10 scaffolds effectively guided and sustained long-term cellular orientation, showcasing a notable and continual improvement in cell alignment along the direction of the grooves.[53] This alignment effect could be particularly advantageous for tissue engineering applications, as aligned cell structures can enhance tissue functionality and integration.[49] The enhanced alignment of hMSCs on these scaffolds may be related to the dimensions of mesenchymal stem cell cytoplasm, which preferentially aligns over grooves within its size range of 10–30 µm.[54,55] However, an increase in the groove size to 80 µm resulted in a decrease in the alignment of hMSCs along the grooves, suggesting that excessively large features may not effectively direct cellular orientation (Figure 5D).

3. Conclusions

This study sought to develop a fabrication approach that combines additive manufacturing with femtosecond laser engraving to create 3D printed scaffolds featuring precise porosity and meticulously controlled surface topography. The integration of these techniques in a single process enabled the fabrication of scaffolds with microgrooves of 10 or 80 µm width and micropits of 25 µm diameter, overcoming current challenges related to surface accessibility, pattern resolution, and debris accumulation. The precision of femtosecond laser engraving significantly improved the reproducibility of surface patterns despite of the engraved layer, while preserving the mechanical and intrinsic properties of the polymeric structure. Remarkably, the engraved patterns retained their morphology for at least 14 d in an aqueous environment, indicating their stability over prolonged incubation times. Furthermore, in vitro evaluation revealed that the geometry of the engraved patterns had a significant impact on the attachment and morphology of hMSCs. Specifically, scaffolds with 10 µm aligned grooves promoted enhanced cell alignment and elongation, which are critical factors for directing cellular function. This work establishes a precise methodology for scaffold fabrication, offering a robust platform to investigate the influence of scaffold structure and topography on cell fate. Future studies will further explore the potential of these scaffolds in creating more complex 3D tissue constructs, including bone scaffolds, where precise microtopography is crucial for facilitating the attachment and growth of osteoblasts, ultimately leading to improved bone integration and healing.

Although the micropatterns in this study are applied only to the top surface of each scaffold layer, integrating these patterns within a 3D-printed scaffold offers distinct advantages over traditional 2D surface patterning. The combination of 3D scaffold architecture and precise surface topography provides a more physiologically relevant environment that may enhance cellular behavior beyond what is achievable with 2D patterns. However, it is important to acknowledge the need for further comparative studies between 2D and 3D-patterned systems to fully understand the advantages of 3D micropatterning for cell attachment and

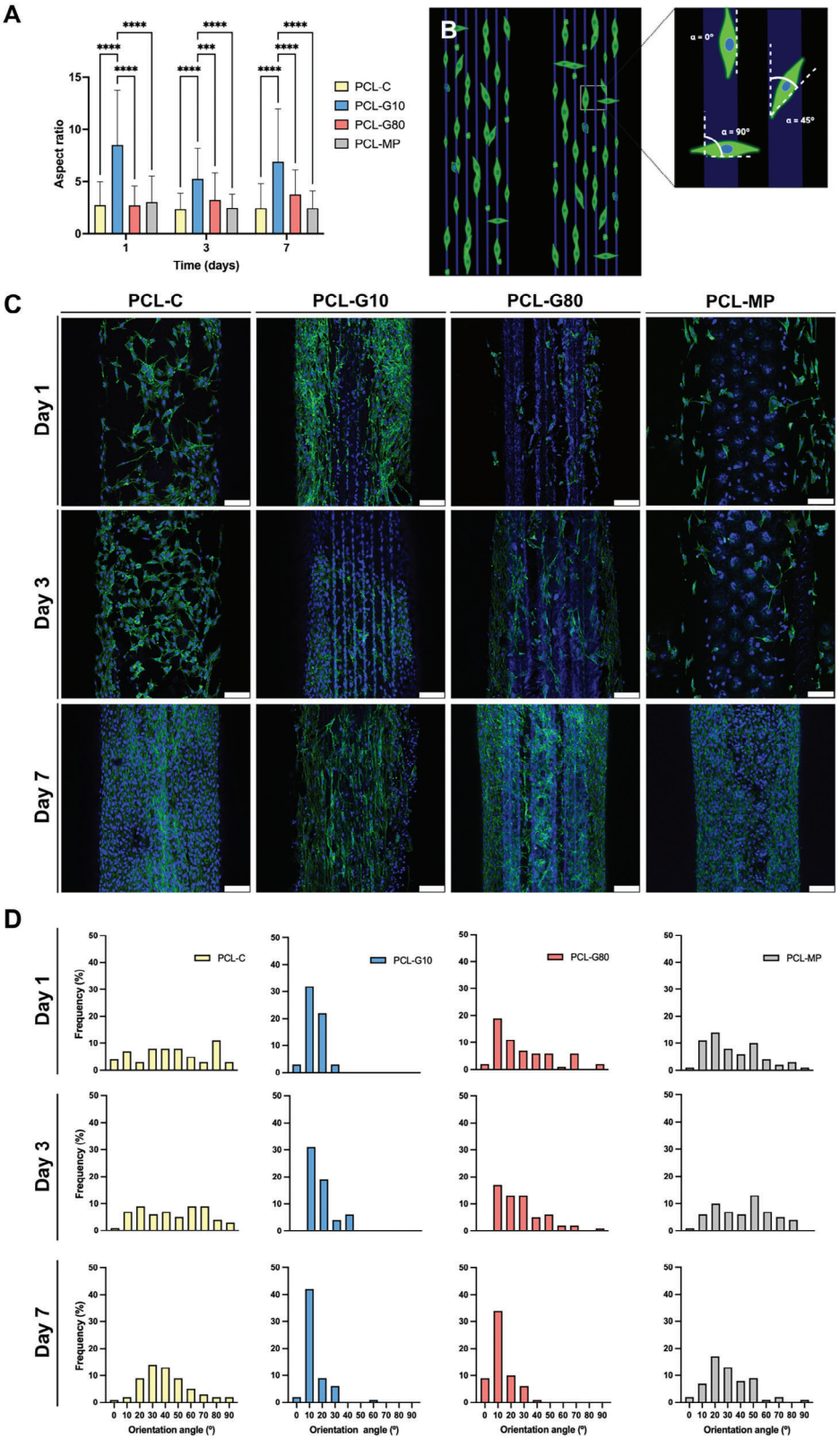

Figure 5. Results from quantification of hMSC organization. A) Cell aspect ratio (major axis/minor axis) measured on isolated cells from engraved and non-engraved scaffolds on day 1, 3, and 7 (*** $p < 0.001$ and **** $p < 0.0001$). B) Schematic representation of the angle measurements obtained with ImageJ on confocal micrographs. C) Micrographs corresponding to 1, 3 and 7 d of culture on engraved and non-engraved scaffolds. Scale bar: 100 µm. D) Frequency histograms of angle distribution on engraved and non-engraved scaffolds at 1, 3, and 7 d of culture.

organization. Future work will focus on these comparisons to elucidate the mechanisms behind the observed effects in cellular responses.

4. Experimental Section

Materials: Poly(ϵ-caprolactone) (PCL; 50 kDa) was obtained from Polysciences (Warrington, PA, USA). Minimum essential medium α (MEM α), fetal bovine serum (FBS), phosphate buffered saline (PBS), penicillin-streptomycin, and TryplE Express were from Gibco (Waltham, MA, USA). 4′,6-diamidine-2′-phenylindole dihydrochloride (DAPI), and Triton X-100 were from Sigma Aldrich (San Luis, MO, USA).

Scaffold Fabrication: Scaffolds (10×10×5 mm) were printed using a Bioplotter Manufacturer controlled by VisualMachines software (EnvisionTec, Germany) from 3D models created using SketchUp (Trimble; Sunnyvale, CA) in.stl format. PCL was heated at 120 °C and printed at 6 bar and 1.7 mm s^{-1} using a 22G nozzle. Models were sliced in 400 µm height layers and patterned as continuous parallel strands with 0.7 mm on-center spacing in a woodpile geometry. After the printing of each layer, the surface of the deposited fibers was engraved using a femtosecond laser.

In this study, three distinct surface patterns were applied to 3D printed PCL fibers: parallel grooves with widths of either 10 µm or 80 µm along the fiber direction, and micropits with a diameter of 25 µm. Non-engraved scaffolds served as controls (PCL-C). Scaffolds with the 10 µm groove pattern (PCL-G10) featured fibers engraved with 7 parallel grooves, spaced 40 µm apart on-center, with a total width of 240 µm. Scaffolds with the 80 µm groove pattern (PCL-G80) had fibers engraved with 3 grooves, spaced 120 µm apart on-center, covering approximately 320 µm in width. Micropit-patterned scaffolds (PCL-MP) featured fibers engraved with four rows of micropits, spaced 67.5 µm apart on-center. Patterns were designed using CAD (Figure 1). Each fiber underwent engraving along an 8 mm length, comprising 80% of the total fiber length. In this study, fiber engraving was carried out using a femtosecond laser system (STELA; Santiago de Compostela, Spain). The selected configuration on the laser operated at low energy output included delivering ultrashort pulses with a 35 fs pulse duration and an energy level of 1 mJ, a repetition rate of 1 kHz, a wavelength of 800 nm, and a bandwidth of 45 nm.

Characterization of Micropatterned Scaffolds: The fiber and pore size, and micropattern dimensions of the scaffolds were analyzed by microcomputed tomography (microCT) and scanning electron microscopy (SEM). Samples from each experimental condition were scanned using a SkyScan 1272 (Bruker; Kontich, Belgium) using a voltage of 50 kV, 200 µA, and no filter at a pixel size of 3 µm was used. The exposure time was 360 ms and rotation step 0.2°. Single fibers were also recorded using a voltage of 40 kV, 190 µA, and no filter at a pixel size of 0.6 µm. The exposure time was 1200 ms and rotation step 0.4°. Scans were reconstructed and analyzed using NRecon and CTAn software. For SEM analysis, scaffolds were previously coated with gold and observed using a FESEM EVO (Zeiss; Oberkochen, Germany).

The surface characterization of engraved fibers was performed with the Sensofar S-NEOX non-contact surface profiler (Sensofar; Barcelona, Spain) on confocal microscopy mode. Briefly, 3D reconstructions of the micropatterned surfaces were obtained using a 50x brightfield magnification objective (optical resolution per technical specifications: X-Y, 0.17 µm; spatial sampling, 0.28 µm; field of view, 340×710 µm), Z-scan measuring system and Autofocus configuration. Then, reconstructions were analyzed with the SensoMAP Advanced Analysis Software to extract the 3D profiles from the topologic layers of the samples.

The stability of the micropatterns on engraved scaffolds (PCL-G10, PCL-G80, and PCL-MP) was evaluated by incubation in PBS at 37 °C. After 14 d, samples were rinsed with water (3x) and dried in a vacuum desiccation. Then, microCT analysis was carried out and the dimensions of the patterns engraved on the surface of the printed fibers were measured at layer 2, 4, and 6, using CTAn software.

Differential Scanning Calorimetry: Crystallization analysis was carried out using a DSC Q100 (TA Instruments, New Castle, DE) equipped with an RCS cooling unit and nitrogen flow (50 mL min^{-1}). Thermograms were obtained at a scanning rate of 10 °C min^{-1} from -20 °C to 200 °C, followed by cooling to -20 °C and again to 200 °C. The second heating cycle was utilized to determine the enthalpy of cold crystallization (ΔH_{cc}), melting temperature (T_m), and enthalpy of melting (ΔH_m). Crystallinity (X_c) was calculated using Equation 1, where ΔH_{mc} denotes the melting enthalpy of 100% crystalline poly(ϵ-caprolactone) (142 J g^{-1}).[56]

$$X_c = \left[\frac{\Delta H_m}{\Delta H_{mc}}\right] \times 100 \quad (1)$$

Gel Permeation Chromatography (GPC): The weight average molecular weight (*Mw*) and number average molecular weight (*Mn*) of PCL scaffolds were determined using gel permeation chromatography (GPC; Waters, Milford, MA) using Waters Ultrastyragel columns equipped with a Waters 410 refractive index detector and a multiangle laser light scattering detector (Treos; Wyatt Technology, Santa Barbara, CA). A sample of ca. 20 mg of the scaffolds (PCL, PCL-G10, PCL-G80, and PCL-MP) was dissolved in 4 mL of tetrahydrofuran (THF) on a shaker table for 24 h. Samples were filtered through PTFE 0.45 µm syringe filters before injection. GPC was performed at a flow rate of 1.0 mL min^{-1}. Data was acquired and processed using the Breeze 3.30 software (Chromatographic Manager; Waters Corporation). Polystyrene standards (range 2800–710 000 Da) were used to obtain a calibration curve by polynomial regression (Tokyo Soda Ltd., Tokyo, Japan).

Tensile Properties Evaluation: The effect of engraving on the tensile properties was evaluated using a texturometer (TA.XTplus Texture Analyzer, Stable Micro Systems; Surrey, UK) with a 5 kg load cell. Individual fibers ($n = 3$) were printed and engraved using the same conditions as described in Scaffold fabrication, and then, subjected to elongation up to 100% strain at a constant rate of 1 mm s^{-1}. Fibers were clamped leaving an initial gap of 15 mm. The obtained data were utilized to derive load–displacement profiles, incorporating the cross-sectional area of each specimen.

hMSCs Seeding on Scaffolds: Human bone marrow-derived mesenchymal stem cell line (hMSCs) obtained from ATCC (PCS-500-012) were cultured in MEM α medium supplemented with 2×10^{-3} M L-glutamine, 10% FBS, and 1% pen-strep. At 80% confluency, hMSCs were tripsinized, counted, and dynamically seeded on the scaffolds. Briefly, engraved and control scaffolds ($n = 5$) were sterilized in ethanol 90% and hydrophilized in serial dilutions of ethanol:PBS (70:30, 50:50 and 30:70) for 30 min each, followed by 3x washing with PBS and further incubation in FBS overnight. Then, scaffolds were transferred into 5 mL syringes with a hMSC suspension (2×10^5 cells per scaffold) and incubated at 37 °C under slow rotation for 6 h. Finally, scaffolds were transferred to non-adherent 48-well plates and incubated in 0.5 mL of culture medium at 37 °C. Cell proliferation was assessed after 1 and 3 days of culture using a CCK-8 assay (Dojindo; Kumamoto, Japan). Briefly, the culture medium was discarded and 200 µL of CCK-8 working solution (containing 10% CCK-8 reagent in 90% culture medium) was added to each well, followed by 3 h incubation. Finally, the media were collected from each well, and absorbance was measured at 450 nm using a Bio-Rad Model 680 spectrophotometer (Bio-Rad; Hercules, CA, USA).

The attachment of hMSCs on engraved and non-engraved scaffolds was evaluated using DAPI staining. Briefly, after 24 h from seeding, samples were washed 3x with PBS and fixed in 4% paraformaldehyde for 30 min. Then, cell nuclei were stained with 1 µg mL^{-1} of DAPI by incubation for 5 min at room temperature. Finally, the samples were washed with PBS and observed in a Leica Stellaris 8 confocal microscope (LEICA; Mannheim, Germany). Cell nuclei present inside the engraved area or equivalent area in the control scaffolds were counted using the confocal imaging software LAS X 3D Analysis for automatic 3D analysis. Micrographs were processed and cropped to adjust the selected area. Then, the number of nuclei on the samples was normalized by the image area to assess differences on cell attachment (defined as hMSCs count per 100 μm^2) in $n = 5$ fields of view.

Nuclei shape analysis, sphericity, Feret's diameter (the longest distance between any two points along the selection boundary) and aspect ratio

(major ellipsoid/minor ellipsoid) were automatically assessed in $n = 60$ cells per field of view with LAS X 3D Image Analysis tool.

Analysis of Cell Orientation: The effect of the micropattern on cellular morphology was assessed by measuring cellular orientation with respect to fiber direction. PCL-G10, PCL-G80, PCL-MP and PCL-C scaffolds were dynamically seeded with hMSCs (2×10^5 cells per scaffold). At 1, 3, and 7 d of culture, scaffolds were washed thrice with PBS and then, cells were fixed using 4% paraformaldehyde for 20 min, permeabilized with 0.1% Triton X-100 in PBS for 10 min, and blocked with 2% bovine serum albumin (BSA) in PBS for 30 min. Then, cell cytoskeleton was stained by incubation with phalloidin-Alexa Fluor 488 for 30 min, followed by PBS washing 3x and incubation with DAPI (1 µg mL^{-1}) for 5 min. Finally, fluorescent micrographs were obtained using a Leica Stellaris 8 confocal microscope (LEICA; Mannheim, Germany).

Cell orientation, defined as the angle between the long axis of the cell and the fiber direction, was measured using ImageJ (NIH; Bethesda, MD) in $n = 5$ images per sample. Briefly, 60 cells per field of view were selected randomly, and their orientation with respect to the reference axis (the vertical axis of the scaffold fibers) was determined. For cell shape analysis, aspect ratio (major axis/minor axis) was measured for each fitted ellipse. Aspect ratio indicated nuclear elongation, with higher values signifying increased elongation. Only individually settled and spread cells were included in the calculations. Cells forming colonies or aggregates were excluded to avoid misleading results.

Statistical Analysis: All data were expressed as mean ± standard deviation (SD). Statistics were analyzed using Graphpad Prism (Graphpad Software, La Jolla, CA). One-way analysis of variance (ANOVA) and Tukey's multiple comparison post-test were used. Differences were considered significant for $p < 0.05$.

Supporting Information

Supporting Information is available from the Wiley Online Library or from the author.

Acknowledgements

This research was funded by MCIN/AEI/10.13039/501100011033 [PID2021-127493OA-C22, PID2022-138322OB-100, and CNS2023-145568] (Spain), Xunta de Galicia [ED431B 2023/07; ED431C 2024/09] and FEDER, EU. L.A.C. and M.P.V. acknowledge Xunta de Galicia for predoctoral fellowships [ED481A-2024-044; ED481A-2023-164]. B.C. acknowledges GAIN/Xunta de Galicia for contract [11-IN606D-2021-2604925]. Y.R.S. acknowledges MCIN (Spain) for contract FPU22/01231.

Conflict of Interest

The authors declare no conflict of interest.

Data Availability Statement

The data that support the findings of this study are available from the corresponding author upon reasonable request.

Keywords

biofabrication, femtosecond laser engraving, micropatterns, tissue engineering, topographies

Received: November 5, 2024
Published online: November 19, 2024

[1] A. T. Nguyen, S. R. Sathe, E. K. F. Yim, *J. Phys.: Condens. Matter* **2016**, *28*, 183001.
[2] S. J. P. Callens, D. Fan, I. A. J. van Hengel, M. Minneboo, P. J. Díaz-Payno, M. M. Stevens, L. E. Fratila-Apachitei, A. A. Zadpoor, *Nat. Commun.* **2023**, *14*, 855.
[3] S. van Helvert, C. Storm, P. Friedl, *Nat. Cell Biol.* **2018**, *20*, 8.
[4] M. Bao, J. Xie, W. T. S. Huck, *Adv. Sci.* **2018**, *5*, 1800448.
[5] N. O. Monteiro, J. F. Fangueiro, R. L. Reis, N. M. Neves, *Bioact. Mater.* **2023**, *28*, 337.
[6] J. Nicolas, S. Magli, L. Rabbachin, S. Sampaolesi, F. Nicotra, L. Russo, *Biomacromolecules* **2020**, *21*, 1968.
[7] A. D. Doyle, K. M. Yamada, *Exp. Cell Res.* **2016**, *343*, 60.
[8] E. Knight, S. Przyborski, *J. Anat.* **2015**, *227*, 746.
[9] B. Yi, Q. Xu, W. Liu, *Bioact. Mater.* **2022**, *15*, 82.
[10] H. Lai, B. Gong, J. Yin, J. Qian, *Mater. Des.* **2022**, *218*, 110663.
[11] L. Iturriaga, K. D. Van Gordon, G. Larrañaga-Jaurrieta, S. Camarero-Espinosa, *Adv. NanoBiomed. Res.* **2021**, *1*, 2100068.
[12] L. Diaz-Gomez, M. E. Elizondo, G. L. Koons, M. Diba, L. K. Chim, E. Cosgriff-Hernandez, A. J. Melchiorri, A. G. Mikos, *Bioprinting* **2020**, *18*, e00076.
[13] M. Malinauskas, S. Rekstyte, L. Lukosevicius, S. Butkus, E. Balciunas, M. Peciukaityte, D. Baltriukiene, V. Bukelskiene, A. Butkevicius, P. Kucevicius, V. Rutkunas, S. Juodkazis, *Micromachines* **2014**, *5*, 839.
[14] S. Ravi-Kumar, B. Lies, X. Zhang, H. Lyu, H. Qin, *Polym. Int.* **2019**, *68*, 1391.
[15] Z. Lin, M. Hong, *Ultrafast Sci.* **2021**, *2021*, 9783514.
[16] R. Suriano, A. Kuznetsov, S. M. Eaton, R. Kiyan, G. Cerullo, R. Osellame, B. N. Chichkov, M. Levi, S. Turri, *Appl. Surf. Sci.* **2011**, *257*, 6243.
[17] A. Daskalova, B. Ostrowska, A. Zhelyazkova, W. Swieszkowski, A. Trifonov, H. Declercq, C. Nathala, K. Szlazak, M. Lojkowski, W. Husinsky, I. Buchvarov, *Appl. Phys. A* **2018**, *124*, 413.
[18] J. Cheng, C. Liu, S. Shang, D. Liu, W. Perrie, G. Dearden, K. Watkins, *Opt. Laser Technol.* **2013**, *46*, 88.
[19] S. Singh, G. L. Samuel, *Silicon* **2023**, *15*, 4229.
[20] A. Daskalova, I. Bliznakova, L. Angelova, A. Trifonov, H. Declercq, I. Buchvarov, *Polymers* **2019**, *11*, 378.
[21] D. Pallarés-Aldeiturriaga, P. Claudel, J. Granier, J. Travers, L. Guillermin, M.-O. Flaissier, P. B. d'Augeres, X. Sedao, *Micromachines* **2021**, *12*, 804.
[22] P. Rougerie, L. Pieuchot, R. S. dos Santos, J. Marteau, M. Bigerelle, P.-F. Chauvy, M. Farina, K. Anselme, *Sci. Rep.* **2020**, *10*, 14784.
[23] J. Lee, S. Chae, H. Lee, G. H. Kim, *Addit. Manuf.* **2020**, *32*, 101023.
[24] A. Omidinia-Anarkoli, R. Rimal, Y. Chandorkar, D. B. Gehlen, J. C. Rose, K. Rahimi, T. Haraszti, L. De Laporte, *ACS Appl. Mater. Interfaces* **2019**, *11*, 7671.
[25] E. Malikmammadov, T. E. Tanir, A. Kiziltay, V. Hasirci, N. Hasirci, *J. Biomater. Sci., Polym. Ed.* **2018**, *29*, 863.
[26] W. Huang, X. Cai, C. Xiao, W. Song, H. Yin, W. Xu, *Heliyon* **2024**, *10*, e26621.
[27] M. Lu, M. Zhang, K. Zhang, Q. Meng, X. Zhang, *Materials* **2022**, *15*, 6771.
[28] R. K. Biswas, N. Farid, B. B. Bhatt, D. Gupta, G. M. O'Connor, P. Scully, *J. Phys. D: Appl. Phys.* **2023**, *56*, 085101.
[29] L. Jiang, A.-D. Wang, B. Li, T.-H. Cui, Y.-F. Lu, *Light Sci. Appl.* **2017**, *7*, 17134.
[30] B. Guo, J. Sun, Y. Lu, L. Jiang, *Int. J. Extreme Manuf.* **2019**, *1*, 032004.
[31] G. Bonamis, E. Audouard, C. Hönninger, J. Lopez, K. Mishchik, E. Mottay, I. Manek-Hönninger, *Opt. Express* **2020**, *28*, 27702.
[32] J. Lim, S. Bupphathong, W. Huang, C.-H. Lin, *Tissue Eng., Part B* **2023**, *29*, 710.

[33] M. S. Aydin, N. Marek, T. Luciani, S. Mohamed-Ahmed, B. Lund, C. Gjerde, K. Mustafa, S. Suliman, A. Rashad, ACS Biomater. Sci. Eng **2024**, In press https://doi.org/10.1021/acsbiomaterials.4c01108.
[34] L. Gemini, S. Al-Bourgol, G. Machinet, A. Bakkali, M. Faucon, R. Kling, *Materials* **2021**, *14*, 2429.
[35] B. Stępak, M. Gazińska, M. Nejbauer, Y. Stepanenko, A. Antończak, *Sci. Rep.* **2019**, *9*, 3069.
[36] G. Ye, W. Wang, D. Fan, P. He, *Appl. Surf. Sci.* **2021**, *538*, 148117.
[37] A. F. Obilor, M. Pacella, A. Wilson, V. V. Silberschmidt, *Int. J. Adv. Manuf. Technol.* **2022**, *120*, 103.
[38] S. 638 American Society for Testing and Materials, *Annual Book of ASTM Standards*, American Society for Testing and Materials, West Conshohocken, PA **2022**.
[39] G. Li, S. Chen, M. Zeng, Y. Kong, F. Zhao, L. Zhang, Y. Yang, *Colloids Surf., B* **2019**, *176*, 341.
[40] W. R. Lykins, D. A. Bernards, E. B. Schlesinger, K. Wisniewski, T. A. Desai, *Polymer* **2022**, *262*, 125473.
[41] Y. Hou, W. Wang, P. Bartolo, *Mater. Des.* **2022**, *216*, 110582.
[42] L. Ghasemi-Mobarakeh, *World J. Stem Cells* **2015**, *7*, 728.
[43] N. Geoghegan, M. O'Loughlin, C. Delaney, K. D. Rochfort, M. Kennedy, S. Kolagatla, L. Podhorska, B. J. Rodriguez, L. Florea, S. M. Kelleher, *Biomater. Sci.* **2023**, *11*, 3077.
[44] H. S. Kim, S. G. Kumbar, S. P. Nukavarapu, *Curr. Opin. Biomed. Eng.* **2021**, *17*, 100260.
[45] X. Zhou, J. Shi, J. Hu, Y. Chen, *Mater. Sci. Eng., C* **2013**, *33*, 855.
[46] M. Werner, S. B. G. Blanquer, S. P. Haimi, G. Korus, J. W. C. Dunlop, G. N. Duda, D. W. Grijpma, A. Petersen, *Adv. Sci.* **2017**, *4*, 1600347.
[47] A. Jana, A. Tran, A. Gill, A. Kiepas, R. K. Kapania, K. Konstantopoulos, A. S. Nain, *Adv. Sci.* **2022**, *9*, 2203011.
[48] L. Pieuchot, J. Marteau, A. Guignandon, T. Dos Santos, I. Brigaud, P.-F. Chauvy, T. Cloatre, A. Ponche, T. Petithory, P. Rougerie, M. Vassaux, J.-L. Milan, N. Tusamda Wakhloo, A. Spangenberg, M. Bigerelle, K. Anselme, *Nat. Commun.* **2018**, *9*, 3995.
[49] S. Liu, J.-M. Yu, Y.-C. Gan, X.-Z. Qiu, Z.-C. Gao, H. Wang, S.-X. Chen, Y. Xiong, G.-H. Liu, S.-E. Lin, A. McCarthy, J. V. John, D.-X. Wei, H.-H. Hou, *Mil. Med. Res.* **2023**, *10*, 16.
[50] Y. He, Y. Yu, Y. Yang, Y. Gu, T. Mao, Y. Shen, Q. Liu, R. Liu, J. Ding, *Bioact. Mater.* **2022**, *15*, 288.
[51] P. Bhattacharjee, B. L. Cavanagh, M. Ahearne, *Sci. Rep.* **2020**, *10*, 6679.
[52] M. T. Doolin, K. M. Stroka, *Tissue Eng., Part C* **2019**, *25*, 662.
[53] M. P. Sousa, E. Arab-Tehrany, F. Cleymand, J. F. Mano, *Small* **2019**, *15*, 1901228.
[54] Y.-T. Yeh, J. Wei, S. Thorossian, K. Nguyen, C. Hoffman, J. C. del Álamo, R. Serrano, Y.-S. J. Li, K.-C. Wang, S. Chien, *Biomaterials* **2019**, *204*, 59.
[55] C. Chen, Y. Zhu, R. Wang, Y. Han, H. Zhou, *J. Healthcare Eng.* **2022**, *2022*, 7179723.
[56] L. Diaz-Gomez, A. Concheiro, C. Alvarez-Lorenzo, C. A. García-González, *Carbohydr. Polym.* **2016**, *142*, 282.